

CHEMICAL IMAGING

Electrochemical imaging of neurotransmitter release with fast-scan voltammetric ion conductance microscopy

Yunong Wang¹, Cristobal Rodriguez², Sasha E. Alden¹, Myung-hoon Choi³, Kristen Alanis¹, Rahul Srinivasan^{2,4*}, Lane A. Baker^{1*}

Understanding the dynamic spatial and temporal release of neurotransmitters can help resolve long-standing questions related to chemical modulation of neurological circuits. Dopamine modulates function in a range of physiological processes and is key to transmission in addiction and neurological disorders. Studies at subcellular scales promise to help develop a broader understanding of dopamine release, diffusion, and receptor activation and how these processes lead to functional outcomes. Electrochemical measurements of dopamine release at individual cells have proven especially informative. We describe incorporation of fast-scan cyclic voltammetry for detection of dopamine release with subcellular spatial resolution and millisecond time resolution. The platform is benchmarked with standard redox probes and then applied to imaging stimulated release from subcellular locations of a coculture of dopaminergic neurons and astrocytes. Voltammetry reveals heterogeneity in release based on time, location, and neuron identity. We believe that this platform ultimately offers a window to understanding neurotransmission in pathophysiological models of disease where cell-cell communication is key.

INTRODUCTION

Neuronal communication relies on intricate signaling pathways enabled by selective release and uptake of neurotransmitters and ions. The release of neurotransmitters is a carefully choreographed process and is temporally and spatially dynamic. Among the major central nervous system neurotransmitters, dopamine release in the striatum is critical for mediating important aspects of motivated behaviors such as reward and movement (1, 2). Regulation of dopamine release at striatal axonal terminals is regulated by local dopamine release from the somatodendritic compartment of dopaminergic (DA) neurons that then act on postsynaptic dopamine type 2 (D2) autoreceptors in DA neurons (3–9). Because this autoregulatory mechanism exerts profound effects on dopamine release in the striatum, consequently influencing important behaviors such as movement and reward, interest exists in developing a detailed mechanistic understanding of somatodendritic dopamine release in native DA neurons, including the type of vesicles mediating release, the subcellular compartments and cellular domains governing release, and the nature of somatodendritic dopamine neurotransmission, i.e., synaptic versus volume transmission (10–12).

A body of work has developed toward understanding neurotransmission at multiple scales, including subcellular scales (13); however, little is known about subcellular, nanoscale aspects of real-time dopamine release from the somatodendritic compartment of native mid-brain DA neurons. In this regard, electrochemistry using microelectrode techniques have proven invaluable for characterizing dopamine release at the interface of single neuron-like cells (14–16). However, most methods to examine neurotransmitter release at small scales have relied

on microelectrodes or optogenetic signaling, and a smaller group of studies have used electrochemical scanning probes to consider local mapping and interrogation of subcellular features. In particular, seminal work from Baur and Wipf has applied carbon fiber microelectrodes in scanning electrochemical microscopy (SECM) configurations to probe neurotransmitter secretion. These studies revealed the possibilities of electrochemical mapping at neurochemistry but suffered from limited resolution due to the electrode size or feedback mechanisms used (15, 17–19). One of the most promising approaches to realize dynamic mapping with electrochemistry is the combination of SECM with scanning ion conductance microscopy (SECM-SICM), where maps of topography and electrochemistry are collected concurrently by using micro-nanoscale probe that has a conductive electrode for recording faradaic electrochemistry via SECM and an open barrel for measuring ion current that provides SICM position control (20–22). A typical SECM-SICM setup entails either spatial mapping with a constant potential on the SECM electrode to determine chemical distribution (but with a low temporal resolution) or conducting single-point amperometric measurements without spatial information. Furthermore, both strategies lack chemical information that can be incorporated through voltammetric measurements. This limitation can be addressed by applying fast-scan cyclic voltammetry (FSCV) and gaining high local concentration sensitivity and high temporal resolution, which has been previously reported and extensively discussed on single-cell studies (23, 24).

To overcome these limitations, we introduce an FSCV-SECM-SICM scanning system and study primary cocultures of mouse mid-brain neurons and astrocytes as shown in Fig. 1A. This system is able to acquire global DA neuronal topography using a fast dynamic hopping-mode scanning protocol and controlling tip-to-sample distance with the SICM barrel. At each pixel, the probe tip is paused near the cell interface. While in the paused position, the SECM barrel applies a continuous FSCV to monitor dopamine firing from the DA neuron. Fabrication of SECM-SICM carbon probes was achieved by pyrolyzing carbon into one barrel of the dual-barrel pipette. To

Copyright © 2024 The Authors, some rights reserved; exclusive licensee American Association for the Advancement of Science. No claim to original U.S. Government Works. Distributed under a Creative Commons Attribution NonCommercial License 4.0 (CC BY-NC).

¹Department of Chemistry, Texas A&M University, College Station, TX 77845-3255, USA. ²Department of Neuroscience and Experimental Therapeutics, Texas A&M University College of Medicine, Bryan, TX 77807, USA. ³Park Systems Inc, Santa Clara, CA 95054, USA. ⁴Texas A&M Institute for Neuroscience (TAMIN), Texas A&M University, College Station, TX 77843, USA.

*Corresponding author. Email: rahul@tamu.edu (R.S.); lane.baker@tamu.edu (L.A.B.)

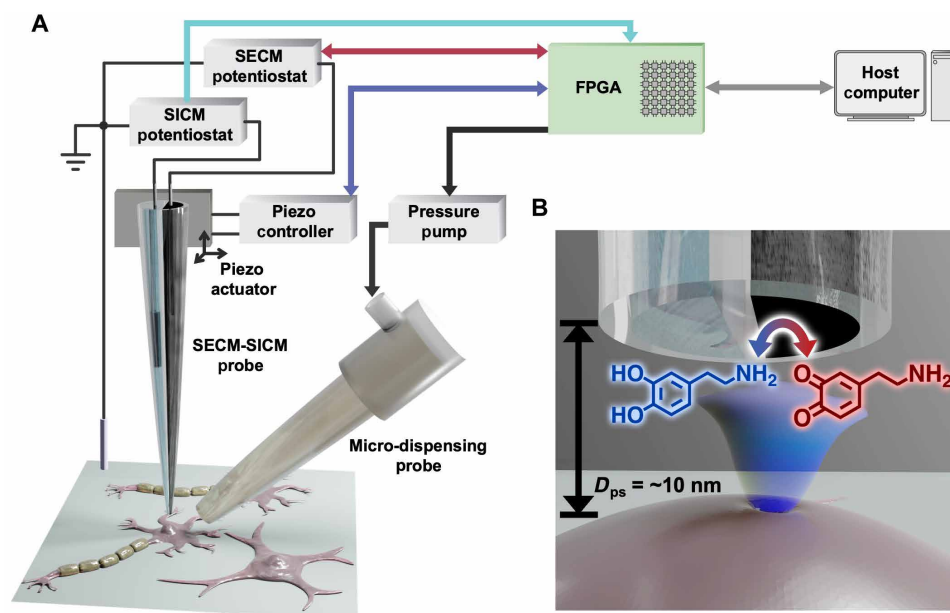


Fig. 1. FSCV-SECM-SICM and scheme of dopamine detection near carbon nanoelectrode. (A) Schematics of the SECM-SICM system. Ion current and redox current at dual-barrel single-sided carbon probe are measured by SICM and SECM potentiostats and sampled by analog-to-digital converters (ADCs) on FPGA. A dosing pipette containing 75 mM KCl is aimed at the target neuron, and injection is controlled by a pressure pump. The piezo actuator, SECM scanning waveform, and dosing event are controlled by FPGA. The topography, dosing pipette injection, and voltammetric data are sent to host PC asynchronously. (B) Triggered dopamine release from the cell is temporally detected through FSCV pulse train at SECM electrode surface with -0.4 -V initial potential, 1.0 -V switching potential at 200 V s^{-1} , and 10 Hz with tip-to-sample distance at $\sim 10\text{ nm}$.

increase the reproducibility of fabricating SECM-SICM carbon probes, an automated carbon probe fabrication system for pyrolyzing dual-barrel pipettes was used (fig. S1) (25). The overall pipette size was controlled to ~ 530 -nm outer diameter (O.D.) with the carbon barrel size of ~ 250 -nm inner diameter (I.D.) after focused-ion beam (FIB) polishing. Neurons were stimulated with concentrated dosing of K^+ from a micro-dispensing pipette ($18\text{-}\mu\text{m}$ I.D.) aimed at the cell body. The increased local concentration of K^+ induced neuron depolarization and the subsequent exocytosis of dopamine (26). Using FSCV-SECM-SICM, we report spatially and temporally resolved exocytosis of dopamine from a DA neuron.

RESULTS

Instrumental principles

The FSCV-SECM-SICM setup is illustrated in Fig. 1A, including the single-sided carbon pyrolyzed dual-barrel nanopipette, which enables the combination of SICM and SECM techniques. For SICM, the empty barrel is filled with electrolyte solution and back-inserted with an Ag/AgCl quasi-reference counter electrode (QRCE). An additional Ag/AgCl electrode was placed into the bath electrolyte solution. When a potential difference is applied between the two electrodes, a steady-state ion current is established due to ion migration through the pipette and the bath solution. When the pipette is lowered toward the sample surface, the pipette access resistance increases due to ion migration hinderance from sample surface, causing a decrease in ion current. Thus, the ion current is used for feedback to control the tip-to-sample distance (27, 28). The SECM barrel uses a nano-disk carbon electrode to study local electroactive species by measuring the faradaic current generated by redox chemistry at the electroactive surface. (29, 30). The SICM barrel was connected to a potentiostat to measure ion current, and the SECM

barrel was connected to another potentiostat through a silver wire to measure faradaic current. A field-programmable gate array (FPGA) was used for overall system control (Fig. 1A). As used here, typically, the SICM barrel was used as positional feedback to suspend the pipette $\sim 10\text{ nm}$ (estimation of tip-to-sample distance is discussed in the Supplementary Materials) away from the sample surface. Notably, tip-to-sample distances reported reflect the separation between the SICM barrel and surface. As the SECM barrel is displaced on the order of $\sim 100\text{ nm}$ laterally from the SICM barrel, errors in estimation of the tip-sample distance under the SECM barrel in areas of the sample that have sharp changes in topography are possible. An FSCV potential waveform was applied to the SECM barrel to detect local secreted chemical concentration over stimulated DA neurons (Fig. 1B).

Mapping of local chemical diffusion

To validate performance of this probe and scanning platform in terms of chemical release detection, a perfusion setup (fig. S2A) with a polyimide (PI) membrane containing $1\text{ }\mu\text{m}$ diameter pores (fig. S2B) was implemented, the setup of which has been previously reported (31). The top and bottom chambers were filled with 100 mM KCl as supporting electrolyte. To study the diffusion of redox probes, the bottom chamber contained 5 mM $[\text{Ru}(\text{NH}_3)_6]\text{Cl}_3$. Diffusion of $[\text{Ru}(\text{NH}_3)_6]\text{Cl}_3$ across the pore from bottom to top chamber served as a spatially confined mimic of local chemical release. The SECM-SICM scanning protocol involves differential cyclic voltammograms (CVs) scanned at 5 V s^{-1} at each pixel. The bulk response (probe retracted) is subtracted from the response recorded when the probe is near the surface (probe extended) (fig. S2C). The differential CV is advantageous due to lower electrode capacitance and signal drift caused by electrode surface changes over time. These differential CV techniques are commonly used in standard carbon fiber

FSCV measurements with the electrode position unchanged (32) and have been used before in electrochemical imaging techniques. The topography map of the PI membrane revealed two pores as shown in fig. S2D, and the differential CVs (fig. S2E) from pixels that corresponded to the pore location in topography (fig. S2D labeled as green A) showed higher $[\text{Ru}(\text{NH}_3)_6]^{3+}$ reduction current (-163.2 pA) compared to a representative location (-3.1 pA) far away from the pore (fig. S2D labeled as green B). To readily compare the two spots, a redox current map was generated by extracting the reduction current at -0.45 V versus Ag/AgCl from each differential CV at each pixel (fig. S2F). We further inferred the concentration of local $[\text{Ru}(\text{NH}_3)_6]^{3+}$ by first collecting a calibration curve of the steady-state reduction current versus $[\text{Ru}(\text{NH}_3)_6]^{3+}$ concentration, measured in a standard electrochemical setup (fig. S2, G and H). Linear fitting was used to convert the redox current map to a local concentration map shown in fig. S2I. This process showed that SECM-SICM was able to measure local concentrations of ~ 0.76 mM $[\text{Ru}(\text{NH}_3)_6]^{3+}$ from flux through the pore, where little to

no $[\text{Ru}(\text{NH}_3)_6]^{3+}$ was measured at points far away from the pore. Overall, this calibration and validation demonstrated the success with the SECM-SICM scanning system to spatially resolve chemical release at ~ 300 -nm spatial scales at micromolar concentrations.

Mapping local chemical depletion

To investigate SECM-SICM detection of changes in local chemical concentration, an Au grid array on top of a glass substrate was fabricated using standard lithography and lift-off techniques (fig. S3, A and B). This Au grid array was placed into chamber (fig. S3C) to isolate 5 mM $[\text{Ru}(\text{NH}_3)_6]^{3+}$ in phosphate-buffered saline (PBS) from the external circuitry. Voltages were applied to alter the chemical environment near the Au grid via a dc power source connected the grid, in addition to the previously discussed SECM-SICM setup (Fig. 2A). A counter driver connected to the Ag/AgCl reference electrode and Pt mesh counter electrode was added to stabilize the reference potential. Measurements were recorded using the same protocol as that for chemical release control experiment to scan over

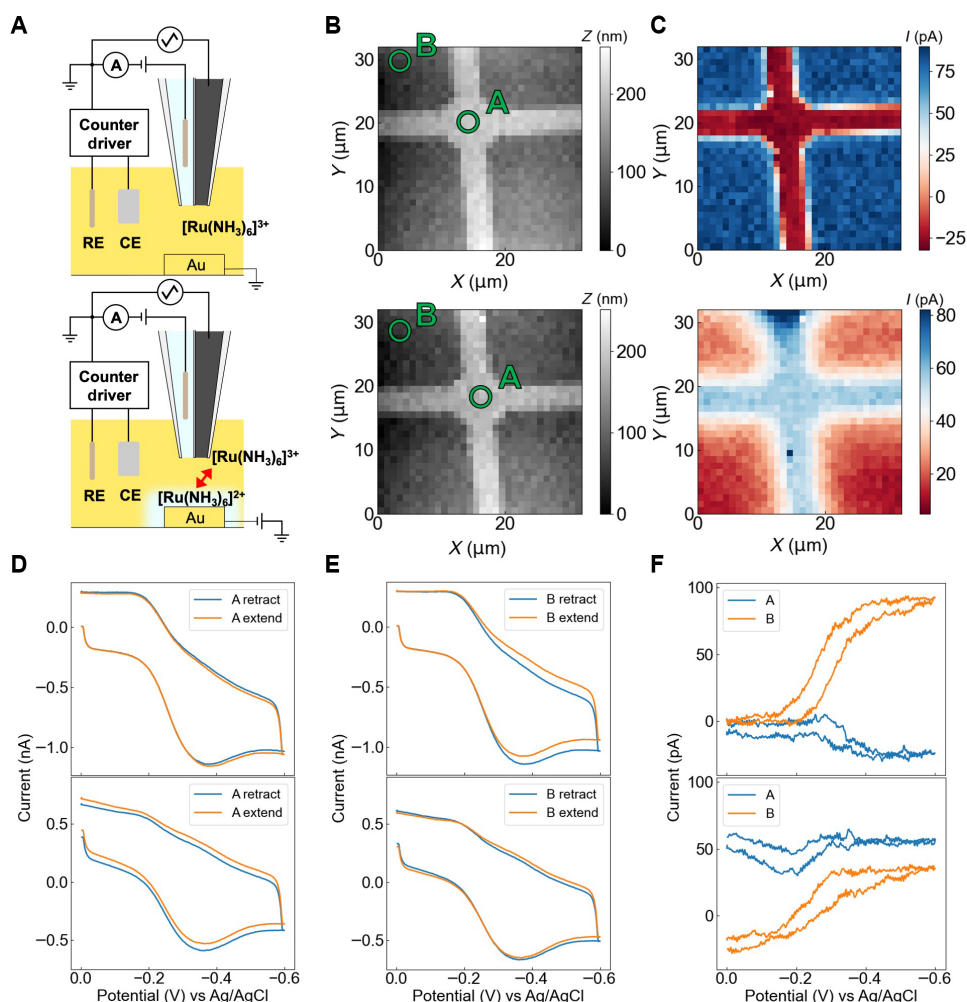


Fig. 2. Measuring chemically resolved depletion processes. (A) Three-electrode SECM-SICM setup with PBS pipette solution ($\text{pH} = 7.4$) and PBS + 5 mM $[\text{Ru}(\text{NH}_3)_6]\text{Cl}_3$ bath solution ($\text{pH} = 7.4$). The SECM barrel scanned CV potential from 0 to -0.6 V versus Ag/AgCl at the scan rate of 20 V s^{-1} . (B) SICM topography, (C) redox current map extracted at -0.5 V versus Ag/AgCl, (D) extended and retracted CV traces over the Au at spot A, (E) extended and retracted CV traces over glass substrate at spot B, and (F) differential CVs at spots A and B. The top figure of each panel illustrates the data of Au substrate at 0 V versus Ag/AgCl, and the bottom figure of each panel shows the data of Au substrate biased at -0.7 V versus Ag/AgCl.

a crossover region of the Au grid (Fig. 2B), where topography and a CV map was collected at 20 V s⁻¹.

SECM-SICM FSCV mapping of the Au grid electrode biased at 0 and -0.7 V was used to investigate the effect on the SECM response during simultaneous substrate chemical reducing or inert conditions, respectively. When the Au grid was grounded, the current map showed an enhanced redox current over the Au electrode, which is due to redox cycling over the conductive Au (Fig. 2, B and C, top maps) (29). The increased amount of [Ru(NH₃)₆]²⁺ generated by carbon probe is re-oxidized at the Au surface when the tip-to-sample distance is small. The enhancement effect can be visualized through extended and retracted CVs (Fig. 2D, top) and differential CV (Fig. 2F, top, trace A). The extracted differential CVs are shown in Fig. 2F top (0 V) and bottom (-0.7 V) for points A and B in Fig. 2B. The reduction current at -0.5 V versus Ag/AgCl over point A was -1.057 and -1.033 nA from the extended and retracted positions, respectively. The current difference between the approached and retracted state was -22 pA, which correlates to the positive feedback mode of the SECM measurement when the Au grid is biased at 0 V (29). On the contrary, SECM measurements over the glass substrate showed substantially smaller reduction current due to the hindered flux of [Ru(NH₃)₆]³⁺ to the carbon electrode, which lead to negative feedback, as shown from the 79 pA difference between the extended (-0.957 nA) and retracted (-1.036 nA) state (Fig. 2, E and F, top). To generate the local depletion of [Ru(NH₃)₆]³⁺, we then turned on the power supply and biased the Au electrode to -0.7 V. Noticeably, the magnitude of differential current at -0.5 V versus Ag/AgCl changed from -22 pA (Fig. 2F, top point A) to 55.9 pA (Fig. 2F, bottom point A) over the Au electrode for the cases of the Au grid biased at 0 and -0.7 V, respectively. This indicates that the positive feedback of the redox current over Au turned to negative feedback, and local depletion was detected when the Au grid was biased at a reductive potential. A similar trend for voltammograms collected over the insulating glass substrate was observed at both Au grid voltages.

Dopamine FSCV detection

Flow cell configurations are routinely used to validate carbon microelectrodes for biomolecule detection during an FSCV experiment (33, 34). Similarly, a program-controlled dopamine (DOP) dosing system was used to qualify the temporal response of the SECM nanoelectrode (fig. S4A). The dosing setup consisted of a micro-dispensing pipette, located ~25 μm away from and at ~45° relative to the SECM-SICM probe, with an external Hepes bath solution. Continuous FSCV was recorded from -0.4 to 1.0 V versus Ag/AgCl at 20 Hz and 200 V s⁻¹ for a total duration of 13 s. At 2.5 and 7 s, injection events (100 ms) of ~580 μM DOP were initiated by the FPGA-controlled pressure valve at 10 kPa. The estimated volume of each injection was 1.42 nl/s, and ~0.14 nl of dopamine solution was dispensed toward the recording pipette for each injection. Figure S4B includes the FSCV spectrogram recorded alongside the pressurized injection trace over the top, where the observed DOP oxidation and reduction peaks were observed at 0.56 and 0.0 V versus Ag/AgCl, respectively. Extracted CVs (fig. S4C) show the clear appearance of a DOP oxidation peak after first injection, in comparison of CVs at 2.5 and 4.0 s. An increase in oxidation current was observed after the second injection due to adsorption of DOP at the carbon electrode surface, visualized in fig. S4C CVs at 4.0 (129.3 pA) and 8.4 s (153.2 pA). Adsorption is also indicated by the current

increase depicted in fig. S5D *i-t* curves, which showed a 28.3 pA increase in peak oxidation current between the first injection peak and second injection peak at 0.6 V versus Ag/AgCl.

Single-point detection on neuronal cell

A large body of work that explores the release of dopamine at cells and tissues exists. In electroanalytical studies at the single-cell scale, neuronal models based on adrenal pheochromocytoma (PC-12) cells have found wide utility in electrochemical cytometry studies using amperometry. In a series of particularly relevant PC-12 studies, FSCV-SECM was investigated by the groups of Baur and Wipf (15, 17–19, 35). These studies showed the possibility of subcellular mapping, albeit with microscale electrodes and relatively crude positional feedback. Subsequent studies by Takahashi (20), Korchev (16, 36–38), and Unwin (16, 22) further developed hybrid SICM-SECM approaches that primarily used amperometric detection at neuronal cells. Here, we use FSCV in a hybrid SICM-SECM format to interrogate genetically modified cells derived from primary cells in coculture with primary astrocytes. Using the dosing pipette configuration previously described, dopamine release was investigated first at a single point near the cell body of modified neurons. The dosing pipette was filled with Hepes buffer containing 75 mM KCl and was injected once the SECM-SICM probe was positioned near the center of a neuronal cell body. An excess amount of extracellular K⁺ triggers depolarizations of the neurons and stimulates the DA neuron to fire dopamine. In comparison, lower amounts or even no dopamine will be emitted by non-DA neurons during this process. Cocultured mouse midbrain neurons and astrocytes served as a well-established model to investigate the firing behavior and the recording capability of the carbon nanoelectrode (39). FSCV-SECM-SICM single-point measurements were collected at 21 neuronal cells, where 11 were DA, and 10 were non-DA neurons. As shown in Fig. 3, mouse midbrain cultures were infected with adeno-associated virus (AAV), which causes the neuron to express the genetically encoded calcium indicator, GCaMP6f, with the control of the human neuron-specific synapsin promoter, hSyn. Therefore, in the presence of Ca²⁺, the DA neurons were tagged green under fluorescence microscopy (Fig. 4A, top) and could be distinguished from the non-DA neurons in the model (Fig. 4A, bottom) (39, 40). Representative SICM topographic maps and single-point FSCV measurement results of a DA (top) and a non-DA (bottom) neuron were shown in Fig. 4 (B and D, respectively). First SICM topographic mapping was scanned at the target neuron (Fig. 4B), then the SECM-SICM pipette was positioned in the soma center and approached, software aimed the micro-dispensing pipette, and lastly an FSCV response was recorded (Fig. 4C) with two 75 mM KCl injection events. Typical differences in voltammetric response based on cell type are exhibited in Fig. 4D. The DA neuron (Fig. 4D, top) showed notably higher and longer duration oxidative current at 0.6 V, with maximal current reaching 100.6 pA during the first injection compared to a non-DA (Fig. 4D, bottom) response of 7.7 pA. Notably, FSCV voltammetry recorded for the non-DA cells following K⁺ injection exhibited a response with little peak splitting, suggesting the possibility of adsorptive processes at the electrode surface. Keeping in mind that this response is background subtracted by the first second of FSCV recording at each pixel, we hypothesize that this is caused by adsorbed proteins or other chemicals secreted from the cell surface as the tip is brought in close proximity to the cell interface. However, these adsorbed species desorbed quickly, as the

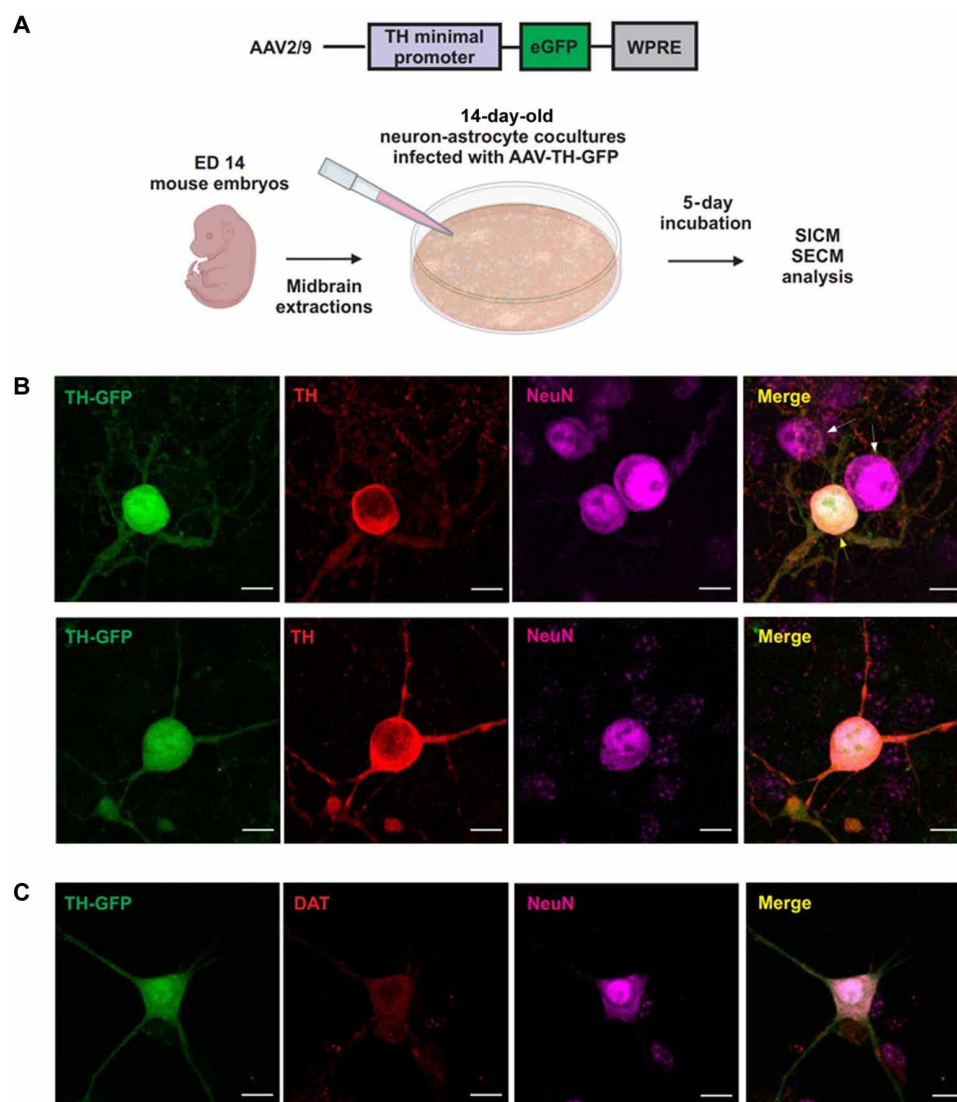


Fig. 3. AAV2/9-TH-eGFP specifically labels live midbrain DA neurons in mouse midbrain neuron-astrocyte cocultures. (A) Two-week old primary DA neuron cocultures were acquired from timed embryonic day 14 (ED 14) midbrain mouse embryos. Cultures were infected with an adeno-associated virus (AAV) with the tyrosine hydroxylase (TH) minimal promoter driving expression of enhanced green fluorescent protein (eGFP) and a Woodchuck Hepatitis virus post-transcriptional regulatory element sequence to stabilize eGFP expression. After a 5-day incubation period to achieve full expression, live cocultures were used for SICM and SECM experiments (B) Fixed and immunostained projected confocal z-stack images showing two examples of GFP-expressing neurons that also express TH and the neuronal marker, NeuN (top and bottom panels). Yellow arrow in the merged image of the top panel points to a GFP, TH, and NeuN expressing DA neuron, while white arrows point to two NeuN-positive midbrain neurons that do not express TH or GFP (C) Fixed and immunostained projected confocal z-stack images showing a GFP-expressing DA neuron that also expresses dopamine transporter (DAT) and the neuronal marker, NeuN; Scale bars, 10 μ m.

current response before dosing at each new cell was always negligible (Fig. 4, C and D, bottom; before injection event and 1.5-s FSCV, respectively).

Statistical analysis of single-point measurements recorded at DA and non-DA cells are shown in Fig. 5, with the voltammetric response shown in left and amperometric response shown in right. A discernable difference is observed between the two populations of cells, but there is also overlap in the error associated with measurements at individual cells. This begins to reveal heterogeneity and variability in measurements recorded with FSCV-SECM-SICM.

FSCV dopamine mapping

To better correlate the distribution of DOP release to the morphology of the DA neuron, optical images were used to guide collection of FSCV-SECM-SICM maps, as shown in Fig. 6. Topography of a DA neuron was first scanned at 500-nm resolution with no electrochemical recording or stimulation to identify regions of interest (Fig. 6B), where the area mapped is indicated by the red box in Fig. 6A. Then, a lower spatial resolution, nominally 2 μ m in XY, hopping mode scan was collected at the same region with a 20-s FSCV recording and a K^+ injection at each pixel. Results showed that the

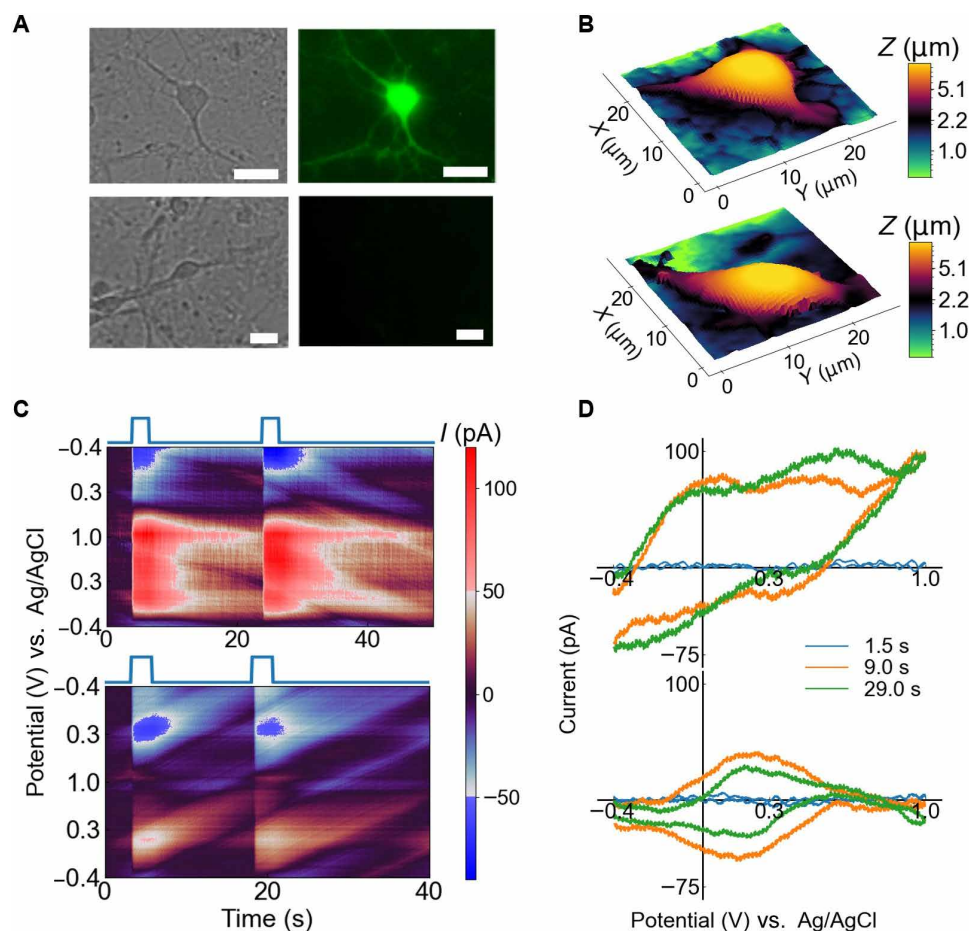


Fig. 4. FSCV single-point measurement of DA/non-DA neuron with K^+ dosing. (A) Bright-field and fluorescence imaging of the target GFP-tagged DA neuron and non-DA neuron without tags. Scale bars, 20 μm . The neurons were in Hepes bath solution (pH = 7.4). (B) SICM topographic imaging of both neurons with 64×64 pixels in a $32 \times 32 \mu\text{m}^2$ region. (C) FSCV spectrogram over the neuronal soma. The two $2.5\text{-s } K^+$ injecting events are shown by the blue trace above the graph. (D) Extracted CVs at 200 V s^{-1} of two neuron types at 1.5, 9.0, and 29.0 s from (C), respectively.

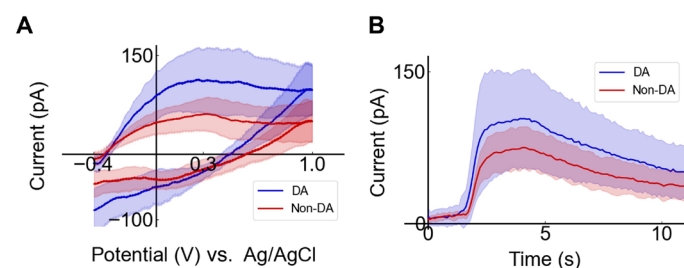


Fig. 5. Statistical analysis of single-point measurement. Averaged (A) background-subtracted FSCV after $\sim 1\text{ s}$ of K^+ dosing and (B) current versus time at $+0.45\text{ V}$ of 11 DA neurons and 10 non-DA neurons. Solid lines represent the mean, and shaded regions (which overlap at some points) on plots represent the SD.

oxidation current map at 0.45 V averaged from 9 to 9.2 s exhibited a higher oxidation current at the soma center (178.1 pA) compared to that of the non-DA neuron (109.1 pA) at the bottom left corner of the image (Fig. 6C). The top DA FSCV response (Fig. 6E) also indicated a larger current response over 100 pA color scale at forward 0.45 V with a maximal peak current at 186.9 pA compared to the bottom non-DA cell with a lower peak current at 103.9 pA. Over the

course of these measurements, carbon electrodes displayed good overall stability (fig. S6). The global neuronal response also is shown as an animation in movie S1, where the topography and electrochemical map at 0.5 V along with FSCV spectrograms at two different pixels (spot A and spot B indicated on the topography image) are presented.

DISCUSSION

To summarize, we have developed an electrochemical imaging solution for characterizing neuronal cell types and mapping single-cell level DA release from mouse neurons. Automated carbon probe fabrication was established producing consistent sized SECM-SICM pipette. Furthermore, we have built an FSCV-SECM-SICM scanning platform and demonstrated its capability to resolve DA firing temporally and spatially, revealing different dopamine release patterns on DA and non-DA neurons.

The present results highlight the possibility of mapping neurochemistry in complex cell models with FSCV-SECM-SICM. Several limitations presently exist that we seek to resolve in the near future. First, the spatial contribution of local stimulation and collection should be quantified with models to better understand signal localization in

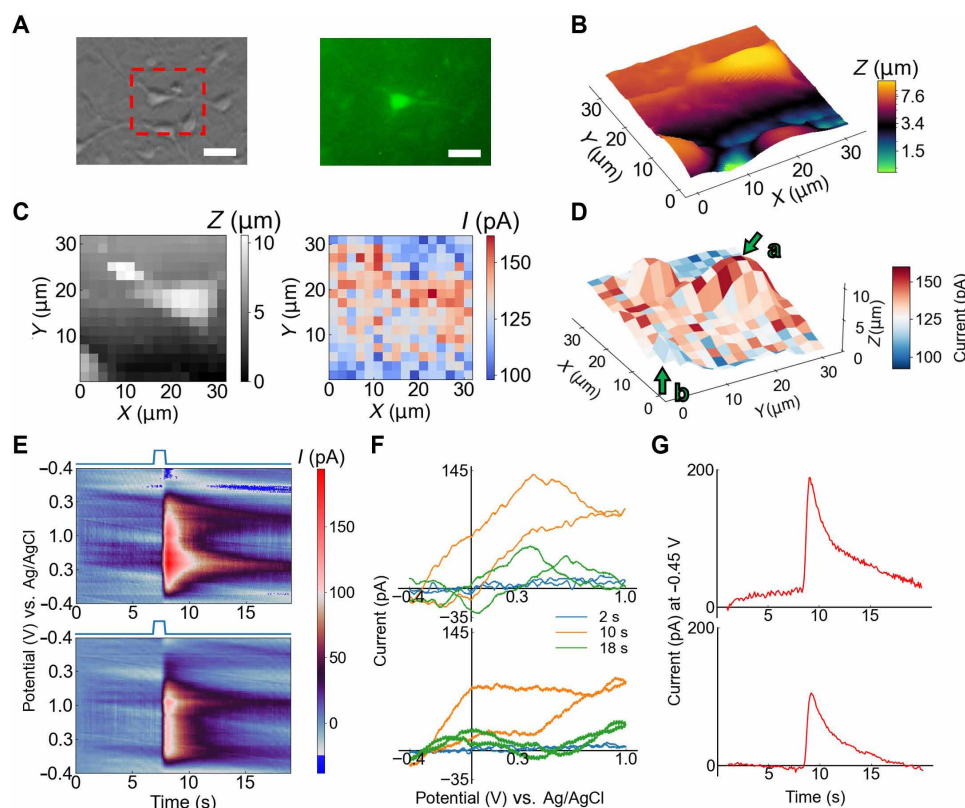


Fig. 6. FSCV mapping of DA neuron. (A) Bright-field and fluorescence imaging of the target DA neuron. Scale bars, 20 μm. (B) SICM topographic imaging of the target neuron with 80 × 80 pixels in a 32 × 32 μm² region. (C) Subsequent FSCV mapping is carried out at the same region to generate 16 × 16 pixel topographic map on the left. At each pixel, the pipette records a 20-s FSCV spectrogram. Oxidation current in each pixel at 0.5 V forward scan, averaged from 9 to 9.2 s, generates an oxidation current map on the right. (D) Topography current-correlated three-dimensional (3D) map. 3D mesh height represents the topography, and the mesh color indicates the oxidation current magnitude. (E) Point FSCV extraction at DA soma (top) and non-DA region (bottom) with one potassium dosing for 1 s. (F) CV at 1, 9, and 17 s and (G) *i-t* trace at +0.45 V forward scan from (E) were extracted, respectively.

measurements, especially with subcellular mapping. Second, variation in signal recorded over different cell types should be analyzed in more detail. We expect that machine learning algorithms might be useful for understanding how signal can be parsed from the two populations in an unbiased manner.

Resolving DA release spatially also reveals an intriguing research direction of probing action potential sensitive spot on neurons, which was previously investigated through fluorescence imaging (41). The possibility to probe local vesicle release directly with voltammetric methods in our study could be used to report on spatial release profiles of multiple electroactive neurotransmitter voltammograms at the same time. Despite the limited dosing amount of K⁺ to each neuron, scanning resolution can be further improved by using a smaller micro-dispensing pipette and decreasing the dosage per injection, which enables a finer potential trigger to the target spot on neurons.

MATERIALS AND METHODS

Midbrain culture preparation and immunostaining

Methods to coculture primary mouse DA neurons and astrocytes have been previously described (39, 40, 42). Briefly, cultures were obtained from embryonic day 14 mouse embryos. Timed-pregnant mice (obtained from Texas A&M Institute for Genomic Medicine) were euthanized via cervical dislocation, and embryos were removed. Embryos

were decapitated, and ventral midbrain was dissected using previously described methods (39, 40). Following dissection, cells were digested in papain for 15 min at 37°C, separated using deoxyribonuclease treatment and mechanical trituration in a stop solution of 10% equine serum in PBS. Cells were plated at a density between 200,000 and 300,000 cells per cover glass on 12-mm circular cover glasses triple coated with poly-L-lysine, poly-L-ornithine, and laminin. After plating, cells were placed in an incubator at 37°C with 5% CO₂ for 1 hour, followed by the addition of 3 ml of neurobasal media supplemented with GlutaMAX, B-27, equine serum, and ascorbic acid as well as penicillin-streptomycin, kanamycin, and ampicillin. Culture medium was exchanged at 3-day intervals, and all primary mouse midbrain neuron-astrocyte cocultures were maintained for at least 3 weeks before performing experiments. Cultures were infected with AAV 2/5 TH-green fluorescent protein 5 days before experiments. For immunostaining, DA cultures were fixed by placing coverslips in 10% formaldehyde/PBS for 40 min. Cultures were permeabilized in 0.01% Triton X-100/PBS and blocked in 10% normal goat serum/PBS solution and incubated with appropriate primary and secondary antibodies. Imaging of immunostained cultures was performed using a confocal microscope (Fluoview 3000, Olympus, Tokyo, Japan) with a 63× and 1.35 numerical aperture (NA) oil-immersion objective (Olympus) at 3× digital zoom. All experiments using mice in this study were approved by the Texas A&M University Institutional Animal Care and Use Committee (IACUC Animal Use Protocol # 2022-0252).

Chemicals and materials

The following Chemicals were used without further purification: potassium chloride (KCl, Sigma Life Science), hexaamineruthenium(III) chloride ($[\text{Ru}(\text{NH}_3)_6]\text{Cl}_3$, Aldrich Chemistry), sodium chloride (NaCl, VWR BDH Chemicals), calcium chloride dihydrate ($\text{CaCl}_2 \cdot 2\text{H}_2\text{O}$, Mallinckrodt Pharmaceuticals), magnesium chloride 6-hydrate ($\text{MgCl}_2 \cdot 6\text{H}_2\text{O}$, Mallinckrodt Pharmaceuticals), D-(+)-glucose (Sigma Life Science), Hepes (Sigma Life Science), sodium phosphate dibasic anhydrous (Na_2HPO_4 , Macron Chemicals), and potassium phosphate monobasic (KH_2PO_4 , J.T.Baker). Chemical release experiments were performed with a custom diffusion cell containing a top and bottom chamber separated by a PI membrane (with 1- μm pore size and 104-pores/ cm^2 density), the preparation of which has been previously reported.

Neuron imaging medium for cell experiments contains 154.18 mM NaCl, 5.00 mM KCl, 1.00 mM CaCl_2 , 0.25 mM MgCl_2 , 2.50 mM D-glucose, and 5.00 mM Hepes. Neuron stimulating medium contains 84.18 mM NaCl, 75.00 mM KCl, 1.00 mM CaCl_2 , 0.25 mM MgCl_2 , 2.50 mM D-glucose, and 5.00 mM Hepes. The pH of both solutions was adjusted to 7.4 before use. All the solution mentioned above used deionized water (18.16 M Ω) from in-lab filtration system (GenPure Pro UV-TOC, Thermo Fisher Scientific).

SECM-SICM probe fabrication

The fabrication of carbon single-sided dual-barrel pipette was divided into two steps: First, the dual-barrel pipette was fabricated using a CO_2 -laser puller (P-2000, Sutter Instruments) with a dual-barrel capillary (1.2-mm O.D., 0.9-mm I.D., 7.5 cm in length; Sutter Instruments) to a ~ 100 -nm O.D. pipette with the following parameter: HEAT = 650, FIL = 3, VEL = 40, DEL = 180, PUL = 155. Then, the pipette was put in a home-built automated carbon probe fabrication system (fig. S1A) to pyrolyze carbon from butane gas flow. The fabrication heating protocol is $\sim 950^\circ\text{C}$ for 1 min, $\sim 500^\circ\text{C}$ for 10 s, and $\sim 670^\circ\text{C}$ for 2 min, and the coil movement protocol is 0.4 mm s^{-1} for pre-pyrolysis, steady for cooling, and 0.1 mm s^{-1} for post-pyrolysis (fig. S1B). The readings from mass flow meters are 23 ml min^{-1} for butane flow, 7 ml min^{-1} for the argon side flow, and 0.15 ml min^{-1} for the argon counter flow.

The pipette was then polished using gallium FIB milling (LYRA-3, Tescan) to form a consistent, solid-filled SECM nano-disk electrode with pipette overall size at 530-nm O.D. The carbon distribution in the pipette was then investigated with energy-dispersive spectroscopy (X-MaxN 50, Oxford Instruments), and the cyclic voltammetry of the carbon barrel was done in 5 mM $[\text{Ru}(\text{NH}_3)_6]\text{Cl}_3$ with 100 mM KCl bath solution using a traditional electrochemical potentiostat setup (CHI-660C, CH Instruments Inc.) (fig. S1, C to E) with Ag/AgCl (3 M KCl, BASi Research Products) as a counter reference electrode.

Micro-dispensing pipette fabrication

Single-barrel pipette was first fabricated from glass capillary (0.95-mm O.D., 0.55-mm I.D., and 127 mm in length; Ace Glass Inc.) using flaming micropipette puller (P-97, Sutter Instruments). The puller parameter is as follows: HEAT = 15, PULL = 0, VEL = 150, TIME = 200, DELAY = 0. Then, the pipette opening was enlarged with the micro-forge stage (Technical Products International Inc.) to 18- μm I.D.

SECM-SICM instrumentation

The SECM-SICM was set up over an inverted optical microscope (Eclipse TE2000-U with DS-Qi1Mc CCD sensor, Nikon) to facilitate

the positioning of the nanopipette and obtain bright-field and fluorescence images (with mercury lamp, M-100T, Chiu Technical Crop.) of DA/non-DA neurons. The optical microscope was placed over an anti-vibrational stage (AVI-200S/LP, Herzan). The pipette movement in the vertical direction was achieved with a stepper motor (M-112.1DG1, Physik Instrumente) for coarse positioning, and a piezoelectric actuator (P-753.21C, Physik Instrumente) for fine positioning, while the pipette fine movement in horizontal direction was driven by a two-axis piezoelectric actuator (P-621.2CL, Physik Instrumente). The dc voltage supply (Model 1786B, BK Precision) was used in the chemical depletion experiment for biasing the Au electrode. Micro-dispensing pipette was pressurized by a pressure valve (TM-200, Narishige) and was attached to a custom-built automated injection system, which consists of a horizontal inertia motor (PD1, Thorlabs Inc.) for coarse positioning, a vertical rotating motor (PDR1, Thorlabs Inc.) for controlling injection angle, and another small linear inertia motor (PD2, Thorlabs Inc.) for fine positioning. The SICM potentiostat (Axopatch 200B, Axon Instrument) and the SECM potentiostat (CHEM-CLAMP, Dagan Corp., with headstage $N = 1$) were connected to the solution barrel and the carbon barrel of the SECM-SICM pipette, respectively. A multichannel oscilloscope (Axon Digidata 1550B, Axon Instrument) connected to the host computer was used to monitor all the analog control and feedback signals. An FPGA board (NI-7845R OEM, National Instruments) was programmed to control all the piezo movement, SECM potential waveform, pressure valve, sample the Faradaic current and ion current, and communicate asynchronously with a home-built LabVIEW (2021, National Instruments) software on the host computer. An SICM approach curve model proposed by Rheinlaender *et al.* (43) was used to estimate the tip-to-sample distance in FSCV single-point and mapping experiments.

SECM-SICM single-point recording and FSCV mapping protocol

For the single-point detection experiment, the micro-dispensing pipette was aimed ~ 35 μm away at the target neuron. The SECM-SICM probe first raster scanned neuron region of interest with a pipette approach rate of 35 $\mu\text{m s}^{-1}$ and retract rate of 60 $\mu\text{m s}^{-1}$ with hopping height of 9 μm and 1.0% ion current threshold to obtain the local topography. The pipette was then positioned over the neuron soma center and approached the surface at 7 $\mu\text{m s}^{-1}$ with 1.5% as the ion current reduction as the threshold. After ion current reached the threshold, the pipette was held in position, and the SECM scanned an FSCV waveform (-0.4 -V initial, 1.0-V switching potential, and scan rate of 200 V s^{-1} at 10 Hz with a four-point averaging filter in real time at each potential step) for a period of ~ 50 s. During the FSCV recording, the FPGA triggered the micro-dispensing pipette injection twice via a 10-kPa pressure pulse for 2.5 s. The pipette was then fully retracted at the rate of 35 $\mu\text{m s}^{-1}$.

For the FSCV mapping experiment, similarly, the injection pipette was aimed at the target neuron (~ 35 μm away), and the same SICM hopping-mode scanning was executed at the region of interest with the same scanning protocol stated in single-point detection experiment to obtain SICM topography map of the target neuron. After topographic imaging, the pipette raster scanned the same region with a lowered resolution, recording an FSCV recording at each XY pixel. The pipette was brought to the surface at 1.5% current threshold with an approach rate of 7 $\mu\text{m s}^{-1}$. A 1-s FSCV (same CV settings as single-point detection) was recorded first to provide a background scan. Subsequently, an FSCV waveform was applied for

19 s, during which KCl was dosed at the eight second by a 10-kPa pressure pulse that lasted for 1 s. After this 19-s period, the pipette was retracted 9 μm from the surface at 35 $\mu\text{m s}^{-1}$ and moved to the next XY pixel, and the process repeated until the map was completed.

In both experiments, neuron topography and FSCV spectrogram data were sent back to the host PC, plotted in real time, and saved as files. Custom Python scripts were designed to analyze and visualize the neuron topography, redox current map, and FSCV responses.

Supplementary Materials

The PDF file includes:

Supplementary Text
Figs. S1 to S6
Legend for movie S1

Other Supplementary Material for this manuscript includes the following:

Movie S1

REFERENCES AND NOTES

- M. O. Klein, D. S. Battagello, A. R. Cardoso, D. N. Hauser, J. C. Bittencourt, R. G. Correa, Dopamine: Functions, signaling, and association with neurological diseases. *Cell. Mol. Neurobiol.* **39**, 31–59 (2019).
- J. D. Berke, What does dopamine mean? *Nat. Neurosci.* **21**, 787–793 (2018).
- P. Palij, D. R. Bull, M. J. Sheehan, J. Millar, J. Stamford, Z. L. Kruk, P. P. A. Humphrey, Presynaptic regulation of dopamine release in corpus striatum monitored in vitro in real time by fast cyclic voltammetry. *Brain Res.* **509**, 172–174 (1990).
- R. T. Kennedy, S. R. Jones, R. M. Wightman, Dynamic observation of dopamine autoreceptor effects in rat striatal slices. *J. Neurochem.* **59**, 449–455 (1992).
- M. Benoit-Marand, E. Borrelli, F. Gonon, Inhibition of dopamine release via presynaptic D2 receptors: Time course and functional characteristics in vivo. *J. Neurosci.* **21**, 9134–9141 (2001).
- P. E. M. Phillips, P. J. Hancock, J. A. Stamford, Time window of autoreceptor-mediated inhibition of limbic and striatal dopamine release. *Synapse* **44**, 15–22 (2002).
- F. Rouge-Pont, A. Usiello, M. Benoit-Marand, F. Gonon, P. V. Piazza, E. Borrelli, Changes in extracellular dopamine induced by morphine and cocaine: Crucial control by D2 receptors. *J. Neurosci.* **22**, 3293–3301 (2002).
- Y. Schmitz, C. Schmauss, D. Sulzer, Altered dopamine release and uptake kinetics in mice lacking D₂ receptors. *J. Neurosci.* **22**, 8002–8009 (2002).
- A. Anzalone, J. E. Lizardi-Ortiz, M. Ramos, C. De Mei, F. W. Hopf, C. Iaccarino, B. Halbout, J. Jacobsen, C. Kinoshita, M. Welter, M. G. Caron, A. Bonci, D. Sulzer, E. Borrelli, Dual control of dopamine synthesis and release by presynaptic and postsynaptic dopamine D2 receptors. *J. Neurosci.* **32**, 9023–9034 (2012).
- M. J. Nirenberg, J. Chan, Y. Liu, R. H. Edwards, V. M. Pickel, Ultrastructural localization of the vesicular monoamine transporter-2 in midbrain dopaminergic neurons: Potential sites for somatodendritic storage and release of dopamine. *J. Neurosci.* **16**, 4135–4145 (1996).
- M. E. Rice, J. C. Patel, Somatodendritic dopamine release: Recent mechanistic insights. *Philos. Trans. R. Soc. Lond. B Biol. Sci.* **370**, 20140185 (2015).
- B. G. Robinson, X. T. Cai, J. X. Wang, J. R. Bunzow, J. T. Williams, P. S. Kaeser, RIM is essential for stimulated but not spontaneous somatodendritic dopamine release in the midbrain. *eLife* **8**, e47972 (2019).
- D. Sames, M. Dunn, R. J. Karpowicz Jr., D. Sulzer, Visualizing neurotransmitter secretion at individual synapses. *ACS Chem. Neurosci.* **4**, 648–651 (2013).
- R. H. Chow, L. von Rüden, E. Neher, Delay in vesicle fusion revealed by electrochemical monitoring of single secretory events in adrenal chromaffin cells. *Nature* **356**, 60–63 (1992).
- R. T. Kurulugama, D. O. Wipf, S. A. Takacs, S. Pongmayteegul, P. A. Garriss, J. E. Baur, Scanning electrochemical microscopy of model neurons: Constant distance imaging. *Anal. Chem.* **77**, 1111–1117 (2005).
- Y. Takahashi, A. I. Shevchuk, P. Novak, B. Babakinejad, J. Macpherson, P. R. Unwin, H. Shiku, J. Gorelik, D. Klenerman, Y. E. Korchev, T. Matsue, Topographical and electrochemical nanoscale imaging of living cells using voltage-switching mode scanning electrochemical microscopy. *Proc. Natl. Acad. Sci. U.S.A.* **109**, 11540–11545 (2012).
- J. M. Liebetrau, H. M. Miller, J. E. Baur, S. A. Takacs, V. Anupunpisit, P. A. Garriss, D. O. Wipf, Scanning electrochemical microscopy of model neurons: Imaging and real-time detection of morphological changes. *Anal. Chem.* **75**, 563–571 (2003).
- D. S. Schrock, J. E. Baur, Chemical imaging with voltammetry-scanning microscopy. *Anal. Chem.* **79**, 7053–7061 (2007).
- D. S. Schrock, D. O. Wipf, J. E. Baur, Feedback effects in combined fast-scan cyclic voltammetry-scanning electrochemical microscopy. *Anal. Chem.* **79**, 4931–4941 (2007).
- Y. Takahashi, A. I. Shevchuk, P. Novak, Y. Murakami, H. Shiku, Y. E. Korchev, T. Matsue, Simultaneous noncontact topography and electrochemical imaging by SECM/SICM featuring ion current feedback regulation. *J. Am. Chem. Soc.* **132**, 10118–10126 (2010).
- Y. Takahashi, A. I. Shevchuk, P. Novak, Y. Zhang, N. Ebejer, J. V. Macpherson, P. R. Unwin, A. J. Pollard, D. Roy, C. A. Clifford, H. Shiku, T. Matsue, D. Klenerman, Y. E. Korchev, Multifunctional nanopores for nanoscale chemical imaging and localized chemical delivery at surfaces and interfaces. *Angew. Chem. Int. Ed. Engl.* **50**, 9638–9642 (2011).
- A. Page, M. Kang, A. Armitstead, D. Perry, P. R. Unwin, Quantitative visualization of molecular delivery and uptake at living cells with self-referencing scanning ion conductance microscopy-scanning electrochemical microscopy. *Anal. Chem.* **89**, 3021–3028 (2017).
- D. J. Leszczyszyn, J. A. Jankowski, O. H. Viveros, E. J. Diliberto Jr., J. A. Near, R. M. Wightman, Nicotinic receptor-mediated catecholamine secretion from individual chromaffin cells. Chemical evidence for exocytosis. *J. Biol. Chem.* **265**, 14736–14737 (1990).
- S. Ge, J. G. White, C. L. Haynes, Critical role of membrane cholesterol in exocytosis revealed by single platelet study. *ACS Chem. Biol.* **5**, 819–828 (2010).
- P. Wilde, T. Quast, H. B. Aiyappa, Y.-T. Chen, A. Botz, T. Tarnev, M. Marquitan, S. Feldhege, A. Lindner, C. Andronescu, W. Schuhmann, Towards reproducible fabrication of nanometre-sized carbon electrodes: Optimisation of automated nanoelectrode fabrication by means of transmission electron microscopy. *ChemElectroChem* **5**, 3083–3088 (2018).
- E. J. Kilbourne, A. McMahon, E. L. Sabban, Membrane depolarization by isotonic or hypertonic KCl: Differential effects on mRNA levels of tyrosine hydroxylase and dopamine β -hydroxylase mRNA in PC12 cells. *J. Neurosci. Methods* **40**, 193–202 (1991).
- P. K. Hansma, B. Drake, O. Marti, S. A. C. Gould, C. B. Prater, The scanning ion-conductance microscope. *Science* **243**, 641–643 (1989).
- C. Zhu, K. Huang, N. P. Siepser, L. A. Baker, Scanning ion conductance microscopy. *Chem. Rev.* **121**, 11726–11768 (2021).
- A. J. Bard, F. R. F. Fan, J. Kwak, O. Lev, Scanning electrochemical microscopy. Introduction and principles. *Anal. Chem.* **61**, 132–138 (1989).
- D. Polcari, P. Dauphin-Ducharme, J. Mauzeroll, Scanning electrochemical microscopy: A comprehensive review of experimental parameters from 1989 to 2015. *Chem. Rev.* **116**, 13234–13278 (2016).
- C.-C. Chen, M. A. Derylo, L. A. Baker, Measurement of ion currents through porous membranes with scanning ion conductance microscopy. *Anal. Chem.* **81**, 4742–4751 (2009).
- J. A. Johnson, C. N. Hobbs, R. M. Wightman, Removal of differential capacitive interferences in fast-scan cyclic voltammetry. *Anal. Chem.* **89**, 6166–6174 (2017).
- E. W. Kristensen, R. L. Wilson, R. M. Wightman, Dispersion in flow injection analysis measured with microvoltammetric electrodes. *Anal. Chem.* **58**, 986–988 (1986).
- A. M. Strand, B. J. Venton, Flame etching enhances the sensitivity of carbon-fiber microelectrodes. *Anal. Chem.* **80**, 3708–3715 (2008).
- J. A. Koch, M. B. Baur, E. L. Woodall, J. E. Baur, Alternating current scanning electrochemical microscopy with simultaneous fast-scan cyclic voltammetry. *Anal. Chem.* **84**, 9537–9543 (2012).
- Y. E. Korchev, Y. A. Negulyaev, C. R. W. Edwards, I. Vodyanov, M. J. Lab, Functional localization of single active ion channels on the surface of a living cell. *Nat. Cell Biol.* **2**, 616–619 (2000).
- P. Novak, C. Li, A. I. Shevchuk, R. Stepanyan, M. Caldwell, S. Hughes, T. G. Smart, J. Gorelik, V. P. Ostanin, M. J. Lab, G. W. J. Moss, G. I. Frolenkov, D. Klenerman, Y. E. Korchev, Nanoscale live-cell imaging using hopping probe ion conductance microscopy. *Nat. Methods* **6**, 279–281 (2009).
- E. V. Sviderskaya, D. J. Easty, M. A. Lawrence, D. P. Sánchez, Y. A. Negulyaev, R. H. Patel, P. Anand, Y. E. Korchev, D. C. Bennett, Functional neurons and melanocytes induced from immortal lines of postnatal neural crest-like stem cells. *FASEB J.* **23**, 3179–3192 (2009).
- E. A. Bancroft, R. Srinivasan, Quantifying spontaneous Ca²⁺ fluxes and their downstream effects in primary mouse midbrain neurons. *J. Vis. Exp.* **163**, e61481 (2020).
- B. M. Henley, B. N. Cohen, C. H. Kim, H. D. Gold, R. Srinivasan, S. McKinney, P. Deshpande, H. A. Lester, Reliable identification of living dopaminergic neurons in midbrain cultures using RNA sequencing and TH-promoter-driven eGFP expression. *J. Vis. Exp.* **120**, e54981 (2017).
- C. Liu, X. Cai, A. Ritzau-Jost, P. F. Kramer, Y. Li, Z. M. Khaliq, S. Hallermann, P. S. Kaeser, An action potential initiation mechanism in distal axons for the control of dopamine release. *Science* **375**, 1378–1385 (2022).
- S. M. Zarate, G. Pandey, S. Chilukuri, J. A. Garcia, B. Cude, S. Storey, N. A. Salem, E. A. Bancroft, M. Hook, R. Srinivasan, Cytisine is neuroprotective in female but not male 6-hydroxydopamine lesioned parkinsonian mice and acts in combination with

17- β -estradiol to inhibit apoptotic endoplasmic reticulum stress in dopaminergic neurons. *J. Neurochem.* **157**, 710–726 (2021).

43. J. Rheinlaender, T. E. Schäffer, An accurate model for the ion current-distance behavior in scanning ion conductance microscopy allows for calibration of pipet tip geometry and tip-sample distance. *Anal. Chem.* **89**, 11875–11880 (2017).

Acknowledgments: Microfabrication was conducted in the Texas A&M University AggieFab Nanofabrication Facility (RRID:SCR_023639), which is supported by the Texas A&M Engineering Experiment Station and Texas A&M University. The Focused Ion Beam (Gallium source, Tescan LYRA-3) was conducted in Texas A&M University Materials Characterization Core Facility (RRID:SCR_022202), which is supported by the Division of Research, the College of Engineering/TEES, and the College of Arts & Sciences, Texas A&M University. **Funding:** This work was funded by National Institute of Neurological Disorders and Stroke (grant/award number: R01NS115809) to R.S. and by the US Army Research Office (W911NF2210051) to L.A.B.

Author contributions: Investigation: Y.W., K.A., S.E.A., and C.R. Methodology: Y.W., M.-h.C., S.E.A., L.A.B., and C.R. Resources: M.-h.C., K.A., S.E.A., L.A.B., R.S., and C.R. Validation: Y.W., L.A.B., R.S., and C.R. Writing—review and editing: K.A., L.A.B., and R.S. Writing—original draft: Y.W. and L.B. Conceptualization: Y.W., L.A.B., and R.S. Formal analysis: Y.W., L.B., and R.S. Software: Y.W. Visualization: Y.W., S.E.A., L.A.B., R.S., and C.R. Funding acquisition: L.A.B. and R.S. Data curation: L.A.B. and R.S. Supervision: L.A.B. and R.S. Project administration: L.A.B. and R.S.

Competing interests: The authors declare that they have no competing interests. **Data and materials availability:** All data needed to evaluate the conclusions in the paper are present in the paper and/or the Supplementary Materials.

Submitted 27 February 2024

Accepted 9 May 2024

Published 11 December 2024

10.1126/sciadv.ado9322